ELSEVIER

Contents lists available at ScienceDirect

## Earth and Planetary Science Letters

journal homepage: www.elsevier.com/locate/epsl





# Migration and accumulation of hydrous mantle incipient melt in the Earth's asthenosphere: Constraints from in-situ falling sphere viscometry measurements

Wen-Yi Zhou a, , Ming Hao b, Rostislav Hrubiak c, Curtis Kenney-Benson , Jin S. Zhang a,

- <sup>a</sup> Department of Geology and Geophysics, Texas A&M University, College Station, TX, USA
- <sup>b</sup> Earth and Planets Laboratory, Carnegie Institution for Science, Washington, DC, USA
- c High Pressure Collaborative Access Team, X-ray Science Division, Argonne National Laboratory, Argonne, IL, USA

ARTICLE INFO

Editor:DR J BADRO

#### ABSTRACT

The Earth's oceanic lithosphere-asthenosphere boundary (LAB) is marked by a notable decrease in seismic wave velocities and an increase in attenuation. This phenomenon is likely attributed to the accumulation of partial melt at the top of the asthenosphere. Nevertheless, the process involving the upward migration and aggregation of low-degree partial melts, highly likely to be mantle incipient melts in the asthenosphere, remains underexplored. Viscosity is a key factor controlling the flow of melts, thus in this study, we used In-situ X-ray falling sphere viscometry experiments to determine the viscosity of the mantle incipient melt containing 1.8–4.0 wt.% water at 1.5–6 GPa and 2100 K. We found that water and pressure can effectively decrease the viscosity of the mantle incipient melt. Therefore, the mantle incipient melts are highly mobile with a high segregation velocity in the deeper part of the asthenosphere. However, during ascent, their mobility diminishes due to an increase in viscosity and a decrease in water content. These mechanisms potentially contribute to the accumulation of partial melt at the top of the asthenosphere.

#### 1. Introduction

The asthenosphere, characterized by low seismic velocities and high attenuation, is a rheologically weak layer under the relatively rigid lithosphere (Chantel et al., 2016; Hua et al., 2023). In particular, near the top of the oceanic asthenosphere (about 100-150 km depths), stronger negative shear wave velocity (Vs) anomaly (normally 5-8% Vs drop) and larger increase of attenuation (>3 orders) have been reported from local and global surface wave and receiver-function studies (e.g. Chantel et al., 2016; Hua et al., 2023). These observations are usually attributed to the presence of a partially molten layer at the top of the asthenosphere. A purely thermal model or grain boundary sliding model is unlikely to account for all these geophysical observations (Mehouachi and Singh, 2018). Global estimation of the partial melt fraction that is needed to account for the strongest seismic velocity reductions at the LAB is ~0.3-0.8 vol% (Table 1) (Audhkhasi and Singh, 2022; Chantel et al., 2016; Freitas et al., 2017), although throughout most of the asthenosphere, melt fraction is relatively low, on the level of 0.1 vol% (Katsura et al., 2017). With such low melt fractions, the melt co-existing with the crystalline upper mantle minerals is chemically closer to the mantle incipient melt rather than mid-ocean ridge basalt (MORB). Moreover, water is highly incompatible, allowing the mantle incipient melt to contain up to a few weight percent of water. Assuming 50–200 ppm water in the ambient oceanic asthenosphere (e.g. Saal et al., 2002), based on experimentally determined water partitioning coefficients between upper mantle minerals and basaltic melt at 3–5 GPa, the mantle incipient melt is estimated to contain 0.5–3.8 wt.% water when melt fraction is close to 0, and contain 0.4–3.2 wt.% water when melt fraction reaches 0.1 vol.% (Tenner et al., 2009).

Viscosity is an important physical parameter that controls the upward migration and aggregation of low-degree mantle incipient melts in the asthenosphere, but unfortunately, the viscosity of mantle incipient melt has never been determined experimentally or computationally. Previous viscosity measurements or calculations on basaltic melts have been mostly focused on the MORB composition (e.g. Sakamaki et al., 2013; Persikov et al., 2018), although a recent study determined the viscosity of a dry primitive alkali basaltic melt (Bonechi et al., 2022). It is noteworthy that primary MORB magmas mainly form through

E-mail addresses: wenyizhou.edu@hotmail.com (W.-Y. Zhou), jinzhang@tamu.edu (J.S. Zhang).

<sup>\*</sup> Corresponding authors.

Table 1
Summary of low velocity anomalies at the off-ridge LAB from seismic observations and corresponding melt fractions.

| Location  | Depth                      | LAB<br>thickness | Oceanic<br>Plate age   | Vs<br>drop | Vp<br>drop  | Method                                 | Reference                                   | Melt fraction using<br>Freitas et al. (2019)'s<br>lab results on Vs | Melt fraction using<br>Audhkhasi and Singh<br>(2022)'s modeling result on<br>Vp |
|---|----------------------------|------------------|------------------------|------------|-------------|--|---|---|---|
| Global  | \                          | \                | \                      | 3–8%       | \           | Surface wave tomography                | Freitas et al. (2019);<br>Romanowicz (1995) | 0.3-0.8 vol% melt   | \   |
| Western U.S.  | 70 km                      | ~20km            | \                      | 15%        | \           | S receiver<br>function                 | Li et al. (2007)                            | 1.5 vol% melt   | \   |
| Pacific Ocean   | 50–90<br>km                | <20 km           | 20–150<br>Ma           | 5–10%      | \           | SS precursors                          | Schmerr (2012)                              | 0.5–1.0 vol% melt   | \   |
| Atlantic Ocean  | 55–75<br>km                | <20 km           | 25–75 Ma               | \          | 5.9<br>(6)% | Active source<br>seismic<br>reflection | Audhkhasi and<br>Singh (2022)               | \   | 1.1 vol% melt   |
| Atlantic Ocean  | 72–88<br>km                | 18–12 km         | 40–70 Ma               | \          | 8.5<br>(4)% | Active source<br>seismic<br>reflection | Mehouachi and<br>Singh (2018)               | \   | 1.4 (8) vol%  |
| Equatorial<br>Atlantic<br>Ocean                           | ~75km                      | \                | 20-80 Ma               | 1–3%       | \           | Surface wave tomography                | Harmon et al. (2020)                        | 0.1–0.3 vol%  | \   |
| Philippine Sea<br>Philippine Sea<br>N.W. Pacific<br>Ocean | 55 km<br>76 km<br>82<br>km | \                | 25Ma<br>49Ma<br>129 Ma | 7–8%       |             | P and S receiver function              | Kawakatsu et al.<br>(2009)                  | 0.7–0.8 vol%  |   |

~10-20% partial melting at shallow (~15-50 km) depths near divergent plate boundaries (e.g. Langmuir et al., 1992; Grove et al., 1992). Such high-degree melting is hardly achieved at greater depth (e.g. in the asthenosphere). What's more, most MORB lavas are chemically evolved, and have experienced variable degrees (3-50 %) of crystal fractionation from the primary MORB magma. Such a process is also unlikely to take place for the mantle incipient melt at depth. Dry primitive alkali basaltic melt, although potentially originating from greater depths compared to MORB, is chemically different from the mantle incipient melt. For example, the  $SiO_2$  content of the primitive alkali basaltic melt is  $\sim 8\%$ higher than that of the mantle incipient melt. More importantly, while the mantle incipient melt in the asthenosphere is likely hydrous, the effect of water on viscosity of silicate melts remains under debate at high pressure-temperature (P-T) conditions. Persikov et al. (2018) suggested that adding water reduces the viscosity of the MORB melt only at pressures ( 4 GPa. At pressures ) 4 GPa, water is found to slightly increase melt viscosity (Persikov et al., 2018), which is in contradiction to what was predicted for hydrous silicate melts from ab initio molecular dynamics simulations in a simplified MgO-SiO2-H2O system up to 32 GPa (Drewitt et al., 2022). Therefore, it is exceedingly important to accurately determine the viscosity of hydrous basaltic mantle incipient melts at high P-T conditions to understand their transportation in the upper mantle.

In this study, we carried out in-situ X-ray falling sphere viscometry experiments on mantle incipient melt with 1.8–4.0 wt.% water from 1.5 GPa to 6 GPa along a 2100 K isotherm. Based on data presented this study and previous studies, we further calculated the mobility and segregation velocities of mantle incipient melt at the oceanic asthenospheric P-T conditions. Our results are important for understanding the melt migration and storage in the upper mantle and origination of the low velocity zone at the top of the asthenosphere.

#### 2. Methods

#### 2.1. Starting materials

We adopted the mantle incipient melt composition given by Davies et al. (2011) and used reagent-grade oxide powders from Sigma-Aldrich for our experiments. We firstly mixed SiO2, Al2O3, CaCO3, Na2CO3, and TiO<sub>2</sub> in appropriate proportions and ground the mixture in a mortar for ~3 h. The mixture was then transferred into a platinum crucible and decarbonated at 1273 K in a high-temperature box furnace for 24 h. The release of CO<sub>2</sub> was confirmed by weighting the mixture before and after heating (Xu et al., 2020). Finally, the SiO<sub>2</sub>-CaO-Al<sub>2</sub>O<sub>3</sub>-NaO-TiO<sub>2</sub> mixture was ground together with FeO, Fe<sub>2</sub>O<sub>3</sub>, and MgO (or Mg(OH)<sub>2</sub>) powders for another 3 h. We prepared three starting materials with different MgO/Mg(OH)<sub>2</sub> proportions (named as MIM L, MIM M, and MIM H), with expected water content ranging from 0 to 4 wt.%. Progressive hydration of fine-grained MgO within the mixed powders during the cross-state sample transportation was possible. Therefore, we quantitatively measured the water content of the final run products using Fourier-Transform InfraRed spectroscopy (FTIR) with details provided in Section 2.3. We also quantitatively measured the chemical compositions of the final run products using Electron Probe Micro-analysis with details shown in Section 2.4 (Table 2).

#### 2.2. In-situ falling sphere viscometry experiments

In-situ X-ray falling sphere viscometry experiments were performed using the VX-3 Paris-Edinburgh (PE) press with the standard cell assembly at the 16 BM-B beamline at the Advanced Photon Source (Argonne National Lab, Illinois). Fig. S1 shows the detailed design of the cell assembly (Kono et al., 2014). The pre-mixed sample powder was

**Table 2**Chemical composition of starting materials and FTIR results on quenched run products.

|            | _                         | -           |             | _           | _                                      |                          |                          |               |               |                       |
|------------|---------------------------|-------------|-------------|-------------|--|--------------------------|--------------------------|---------------|---------------|-----------------------|
| Name       | Na <sub>2</sub> O<br>wt.% | MgO<br>wt.% | CaO<br>wt.% | FeO<br>wt.% | Al <sub>2</sub> O <sub>3</sub><br>wt.% | SiO <sub>2</sub><br>wt.% | TiO <sub>2</sub><br>wt.% | Total<br>wt.% | Water<br>wt.% | Ref.                  |
| MIM_L      | 2.5(1)                    | 13.6(2)     | 10.84(4)    | 9.4(2) *    | 13.1(1)                                | 46.0(3)                  | 2.08(9)                  | 97.5(3)       | 1.8(2)        | This study            |
| $MIM_M$    | 2.38(6)                   | 14.4(2)     | 10.42(5)    | 9.4(1) *    | 13.2(1)                                | 45.5(2)                  | 2.35(4)                  | 97.6(4)       | 2.7(3)        |                       |
| MIM_H      | 2.23(2)                   | 14.67(8)    | 10.17(6)    | 9.2(1) *    | 12.78(8)                               | 43.5(2)                  | 2.2(1)                   | 94.7(2)       | 4.0(3)        |                       |
| MORB       | 2.7                       | 7.9         | 11.6        | 9.9         | 15.9                                   | 51.5                     | 2.7                      | 99.5          | Not measured  | Sakamaki et al., 2013 |
| Peridotite | NA                        | 37.1(9)     | 3.6(2)      | 8.7(3)      | 4.3(3)                                 | 46.6(4)                  | NA                       | 100           | Not measured  | Liebske et al. (2005) |

<sup>\*:</sup> Fe<sup>2+</sup>/Total Fe≈0.9.

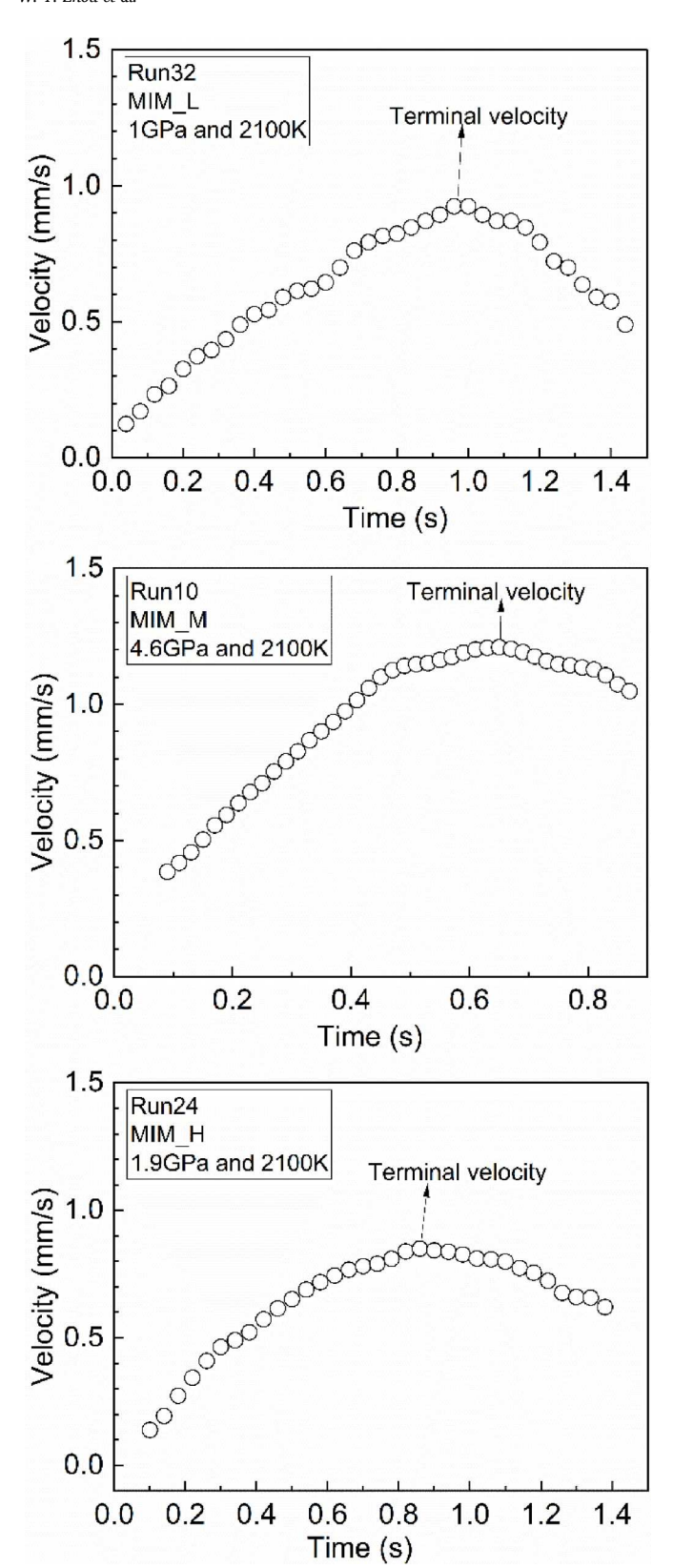


**Fig. 1.** The sphere falling velocity change as a function of time in 3 representative runs during in-situ X-ray falling sphere viscometry experiments.

pressed in a cylindrical die set to form a sample cylinder measured 1.6 mm in height and 1.5 mm in diameter, and a small sample disk with the same diameter but only 0.4 mm thick. The sample cylinder was then loaded into the graphite capsule. A small Re sphere measured  $\sim$ 70–150

 $\mu m$  in diameter was placed at the top of the cylinder, and then covered by the sample disk on top. The external BN capsule was employed to isolate the sample capsule from the graphite heater.

After compressing the loaded cell to the target pressure, to ensure the Re sphere started falling at the targe temperature, we firstly increased temperature gradually to 1073 K from 300 K in roughly 15-20 min, then increased temperature abruptly from 1073 K to 2100 K by adjusting the input power to the target value corresponding to 2100 K according to the pre-calibrated power-temperature curve (Kono et al., 2014). The power adjustment took place very fast and was followed by the Re sphere falling down to the bottom of the sample capsule. MgO was used as the pressure marker, and the pressure uncertainty was estimated to be  $\sim 0.2$ GPa based on MgO equation of state (Kono et al., 2010). The target temperature of 2100 K is 200-700 K above the liquidus of various basalts at 1.5-6 GPa (Bonechi et al., 2022; Yasuda et al., 1994). Temperature uncertainty is estimated to be ~100 K. Complete melting of samples was also confirmed by the straight descent of Re spheres, and the disappearance of sample X-ray diffraction (XRD) peaks during the experiments. Parallel beam polychromatic X-rays were used for imaging the sample chamber. A high-speed camera (Photron FASTCAM SA3) with 1000 frames per second was used to capture the sample chamber images during the sphere falling process. By analyzing the position of Re spheres using ImageJ software, we can calculate sphere falling speeds in each successful run.

We calculated viscosity ( $\eta$ ) with the Stokes equation including the correction factors for the effect of wall (F) and for the end effect (E) (Kono et al., 2014):

$$\eta = \frac{gd_s^2(\rho_s - \rho_l)F}{18\nu E} \tag{1}$$

$$F = 1 - 2.104 \left(\frac{d_s}{d_l}\right) + 2.09 \left(\frac{d_s}{d_l}\right)^3 - 0.95 \left(\frac{d_s}{d_l}\right)^5$$
 (2)

$$E = 1 + \frac{9d_s}{16Z} + \left(\frac{9d_s}{16Z}\right)^2 \tag{3}$$

where g is gravitational acceleration,  $\nu$  is the maximum sphere falling speeds (terminal velocities) calculated from the velocity-time curves given by the images taken by the high-speed camera (Fig. 1).  $d_s$  is the diameter of the Re sphere, which is measured by X-ray radiography. Z is the height of the sample chamber. The sample chamber sizes at all experimental P-T conditions are listed in Table S1.  $\rho_s$  and  $\rho_l$  are the densities of Re sphere and mantle incipient melt, which are calculated by equation of state of Re (Zha et al., 2004) and the density model of hydrous silicate melt constrained by Ueki and Iwamori (2016), respectively. The choice of references for calculating the melt density has little influence on the viscosity calculation due to the large difference in densities between Re (21.02 g/cm3 at ambient condition) and basaltic melt ( $\sim$ 3 g/cm<sup>3</sup>). For example, varying the melt density by 10% would only change the viscosity by <2%. The uncertainty of Re sphere size from X-ray radiographic imaging is  $\pm 2~\mu\text{m},$  resulting in 1–5% uncertainty in viscosity. The overall uncertainty of the obtained viscosity value is <10 %. The sample was finally quenched to ambient temperature by switching the heater off, and then followed by decompression to ambient conditions.

#### 2.3. Fourier-Transform infrared spectroscopy (FTIR)

We double-side polished quenched glass run products into thin pellets with  $30{\text -}100\,\mu\text{m}$  thickness, which were used for the subsequent FTIR measurements. Bubbles were not observed in the quenched glass due to high water solubility of basaltic melts under high pressures (Mitchell et al., 2017). The FTIR analysis was carried out using a Bruker Hyperion II FTIR microscope equipped with a 15X Cassegrain objective, a KBr beam splitter, and a liquid  $N_2$ -cooled mercury cadmium telluride

**Table 3**Experimental conditions and viscosity measurement in this study.

| Starting<br>materials | Run<br>number | Water<br>content of | Pressure<br>(GPa) | Temperature<br>(K) | Viscosity<br>(Pa S) |
|-----------------------|---------------|---------------------|-------------------|--------------------|---------------------|
|                       |               | run<br>products     |                   |                    |                     |
| MIM_L                 | Run32         | \                   | 1.0(2)            | 2100(100)          | 0.215               |
|                       | Run23         | 1.7(1)              | 1.5(2)            | 2100(100)          | 0.240               |
|                       | Run1          | 1.8(1)              | 2.1(2)            | 2100 (100)         | \                   |
|                       | Run16         | 1.8(2)              | 2.7(2)            | 2100(100)          | 0.164               |
|                       | Run6          | \                   | 4.1(2)            | 2100(100)          | 0.121               |
|                       | Run28         | \                   | 5(2)              | 2100(100)          | 0.086               |
|                       | Run38         | \                   | 5.5(2)            | 2100(100)          | 0.215               |
| MIM_M                 | Run29         | 2.6(2)              | 1.8(2)            | 2100(100)          | 0.133               |
|                       | Run3          | 2.8(2)              | 3(2)              | 2100(100)          | 0.082               |
|                       | Run33         | \                   | 4.5(2)            | 2100(100)          | 0.096               |
|                       | Run10         | \                   | 4.6(2)            | 2100(100)          | 0.137               |
| MIM_H                 | Run24         | \                   | 1.9(2)            | 2100(100)          | 0.131               |
|                       | Run5          | \                   | 3.1(2)            | 2100(100)          | 0.082               |
|                       | Run8          | \                   | 4.2(2)            | 2100(100)          | 0.057               |
|                       | Run30         | \                   | 4.5(2)            | 2100(100)          | 0.053               |
|                       | Run37         | 4.0(3)              | 5.7(2)            | 2100(100)          | 0.046               |

detector. The unpolarized infrared light was focused on to the sample with a spatial resolution of 5  $\mu m$ , and FTIR spectra were then collected under transmission mode from  $4000~cm^{-1}$  to  $1000~cm^{-1}$  for 128 scans for each spectrum obtained. The data was processed using the Bruker OPUS software.

The water content  $C(H_2O)$  in glass is determined by the Beer-Lambert Law (Sossi et al., 2023):

$$C(H_2O)(wt\%) = 100 \frac{I_{3550}M(H_2O)}{d\rho_{glass}\varepsilon_{3550}} \tag{4} \label{eq:condition}$$

Here,  $I_{3550}$  refers to the measured absorbance of the IR-active band at 3550 cm<sup>-1</sup> produced by OH<sup>-</sup> and molecular H<sub>2</sub>O stretching modes (Stolper, 1982),  $M({\rm H_2O})$  (=18.015 g/mol) means molar mass of H<sub>2</sub>O, d (cm) refers to glass thickness. For the molar absorption ( $\varepsilon_{3550}$ ), 59,200 cm<sup>2</sup>/mol is adopted based on molar absorption of alkali basaltic and basanitic glass determined by Shishkina et al. (2014). Glass density  $\rho_{glass}$  was calculated from the densities of hydrous basaltic glasses measured in Yamashita et al. (1997).

We mapped water content distribution in 3 representative glass samples quenched from Run 16, Run 29, and Run 37 based on 150–300 single-point FTIR analysis. We also acquired single-point measurements for other run products (Run 1, Run 3). Most sample cells collapsed during the decompression processes, so we were only able to perform FTIR experiments on those 5 well-preserved run products. The measured water content for multiple run products with the same starting materials is consistent, as shown in Table 3. MIM\_L, MIM\_M, and MIM\_H contain 1.8 (2) wt.%, 2.7 (3) wt.%, and 4.0 (3) wt.% water, respectively. As shown in the water content mapping results in Fig. 2, the water distribution in the sample is fairly uniform, suggesting little reaction between graphite capsule and melts, which is expected due to the short duration of each experimental run (< 15 s).

#### 2.4. Electron probe micro-analysis

We employed the CAMECA SXFive Elect at Materials Characterization Facility at Texas A&M University to analyze the chemical compositions of 3 representative quenched glass run products (Run 16, Run 29, Run 37) (Table 2). The element standards include Albite for Na, Ilmenite for Ti, Chromite for Cr, Spessartine for Mn, and the Smithsonian Basaltic Glass from the Juan de Fuca Ridge for Mg, Al, Si, Ca, and Fe. The accelerating voltage was 15 kV and the beam current was 10 nA during experiments. To obtain the average chemical composition of each run product, we performed measurements at 10 randomly selected positions and got similar results, suggesting the homogeneity of the run products.

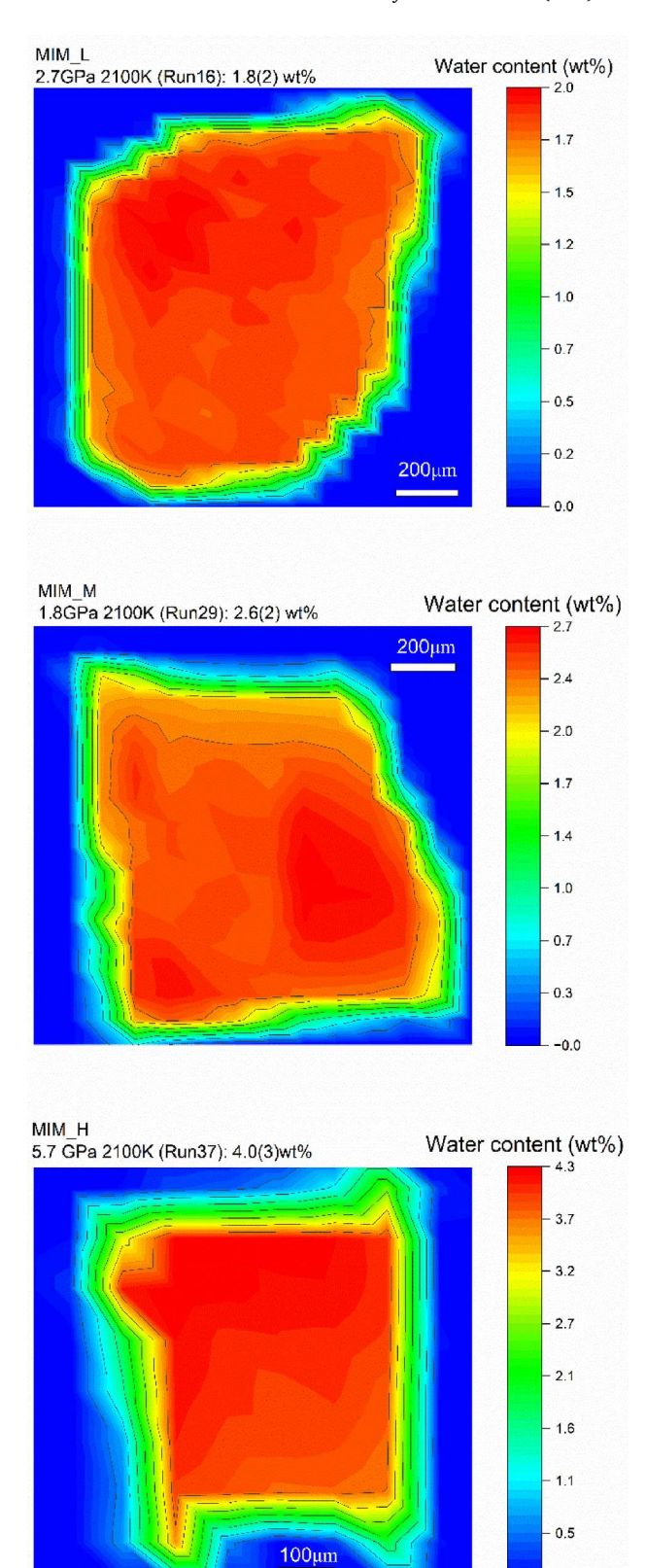


Fig. 2. Water content map for 3 quenched run products based on FTIR measurements.

#### 2.5. Melt segregation velocity modeling

The segregation velocity  $(V_m)$  of mantle melt from the solid matrix, based on Darcy's law, is given by:

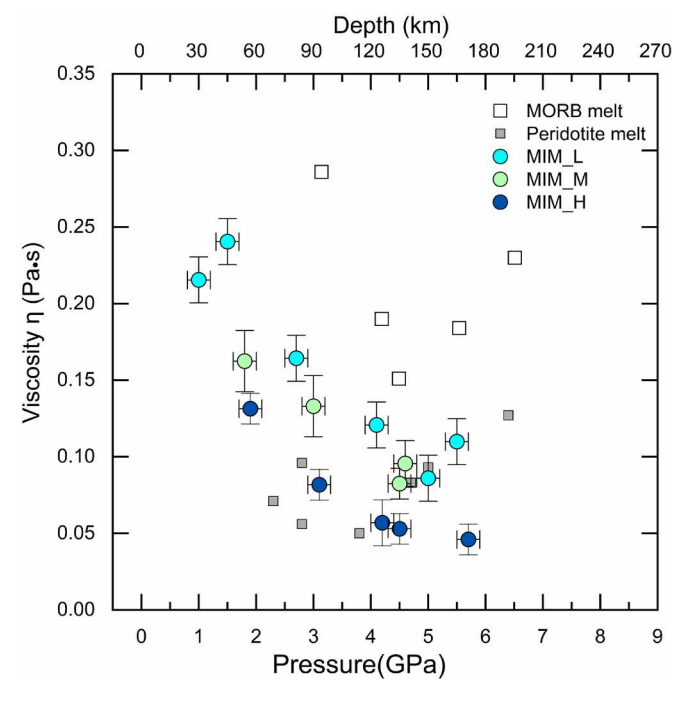


Fig. 3. Viscosity  $(\eta)$  of mantle incipient melts in this study along a 2100(100) K isotherm. For comparison, the viscosity of the MORB melt at 2000–2100 K (Sakamaki et al., 2013) and the viscosity of the peridotite melt along a 2100 (50) K isotherm are also plotted.

$$V_m = \frac{k \cdot \Delta \rho \cdot \mathbf{g}}{\varphi \cdot \mu} \tag{5}$$

Where  $\Delta \rho$  is the density contrast between the melt and surrounding solid mantle, g is the gravitational acceleration value (9.8 m/s<sup>2</sup>),  $\varphi$  is the melt fraction, and  $\mu$  is the melt viscosity. The permeability (k) of melt can be calculated as follows (Connolly et al., 2009):

$$k = \frac{d^2 \varphi^n}{C} \tag{6}$$

Where d is the mineral grain size and C are numerical constants that depend on the melt network geometry. Based on permeability simulations on olivine-basalt aggregates with low melt fraction down to  $\sim$ 2%, Miller et al. (2013) obtained n = 2.6 and C = 56, which were used in this study. The parameter values (e.g., d,  $\varphi$ ) used in this study are shown in the captions of Fig. 4-6. The assumed melt fraction is 0.1 vol% in Fig 4-6, since 1 vol% melt is likely to exist in the regions immediately adjacent to the LAB where strongest seismic velocity anomaly is observed (Table 1, Supplementary Text 1). 0.1 vol% melt is more realistic throughout most of the asthenosphere (Katsura et al., 2017). It is noteworthy that the melt fraction was assumed to be independent of depth when calculating the melt segregation velocity model in this study. Since the water concentration in the melt and the melt fraction are likely to decrease and increase during its ascent, quantification of their combined effects on the melt transport properties remains challenging. Thus, in this study, we chose to fix the melt fraction as 0.1 vol% and only vary the water content in the melts to focus on the effect of water content on melt transport properties. To illustrate the melt migration scenarios when higher melt fractions are expected, we also calculated the melt segregation velocity with 1 vol% melt fraction, which is ~1 order higher than that with 0.1 vol% melt fraction (Fig. S2). Future experimental and theoretical investigations considering the change of both melt fraction and water contents across the entire asthenosphere will be needed to fully characterize the melt migration process in this region.

#### 3. Results and discussion

As shown in Fig. 3, we plotted the viscosity of the 3 hydrous mantle incipient melts (MIM\_L, MIM\_M, MIM\_H) and compared with dry MORB and dry peridotite melts at similar P-T conditions (Liebske et al., 2005; Sakamaki et al., 2013). The hydrous mantle incipient melts are less viscous than MORB melt, but more viscous than peridotite melt at pressures less than 4 GPa. At higher pressures, the viscosity of peridotite melt surpasses hydrous mantle incipient melts. The effect of pressure on the viscosity of the mantle incipient melts is not monotonic. As shown in Fig. 3, the viscosity of the MIM\_L melt (1.8 wt.% water) decreases with pressure and reaches a minimum at ~5 GPa. This trend aligns with the finding reported by Sakamaki et al. (2013) for the MORB melt, where a viscosity minimum was observed at ~4 GPa. The viscosity of the peridotite melt shows a similar trend with a minimum at ~4 GPa, although it was not discussed in Liebske et al. (2005). The observed viscosity minimum of silicate melts at 4–5 GPa appears to correspond with the highest cation diffusivity at ~5 GPa (Wang et al., 2014). The initial impact of pressure (<5 GPa) on silicate melts is to decrease viscosity by reducing the T-O-T angle, consequently depolymerizing the melt structure. However, as pressure increases beyond 5 GPa, the tetrahedral packing fraction limit is reached, leading to an increase in coordination and resulting in a positive dependence of viscosity on pressure (Wang et al., 2014). For the MIM\_H melt (4.0 wt.% water), although a viscosity minimum is not observed within the explored pressure range (1.5-6 GPa), the pressure derivative of viscosity  $(d\eta/dP)$  is notably smaller at 5-6 GPa compared with the value at lower pressures. This indicates that the tetrahedral packing fraction limit might be approached at 6 GPa or at a slightly higher pressure than 6 GPa. To further investigate the viscosity minimum for the MIM\_H, future studies at higher pressures will be necessary. Drewitt et al. (2022) reported a monotonic increase in viscosity with pressure at 0-32 GPa in a simplified MgO-SiO2-H2O basalt system based on ab initio molecular dynamics simulations, which is different from what was observed in this study and previous studies (Liebske et al., 2005; Sakamaki et al., 2013).

It is not surprising that adding water decreases viscosity of the mantle incipient melts. By depolymerizing the melt structure through the formation of hydroxyl units from the reaction between water and the bridging oxygen atoms, water decreases melt viscosity (Kohn, 2000). As shown in Fig. 3, adding 1 wt.% water could decrease the viscosity of the mantle incipient melts by about 14%, which is 7 times more than the predicted 2-3% viscosity decrease caused by addition of 1 wt.% of water in a simplified MgO-SiO<sub>2</sub>-H<sub>2</sub>O basalt system (Drewitt et al., 2022). Another theoretical modeling study by Persikov et al. (2018) suggested that viscosity reduction resulted from addition of water is significant at pressures < 4 GPa, but at higher pressures, water would slightly increases the viscosity. The discrepancies between this study, Persikov et al. (2018), and Drewitt et al. (2022) are likely caused by the compositional difference (mantle incipient melt vs MORB vs MgO--SiO<sub>2</sub>-H<sub>2</sub>O system) and the use of different methods (experiments vs structural-chemical theoretical model vs ab initio molecular dynamics simulations).

In summary, our results suggest that increasing pressure (< 5 GPa) and water content both decrease viscosity of mantle incipient melts.

# 4. Implications for melt migration and accumulation in the asthenosphere

The temperature in our experiments is 100–500 K higher than the temperatures expected in the asthenosphere under a 70 Ma old oceanic plate (Fig. 4a) (Sakamaki et al., 2013). Assuming the viscosity of MORB and the mantle incipient melts share similar temperature dependance (Sakamaki et al., 2013), we calculated the depth dependent viscosity profile of MIM\_L with 1.8 wt.% water and MIM\_H with 4.0 wt.% water along the geotherm shown in Fig. 4a. We found that viscosity drops quickly with increasing depths in the asthenosphere and reaches a

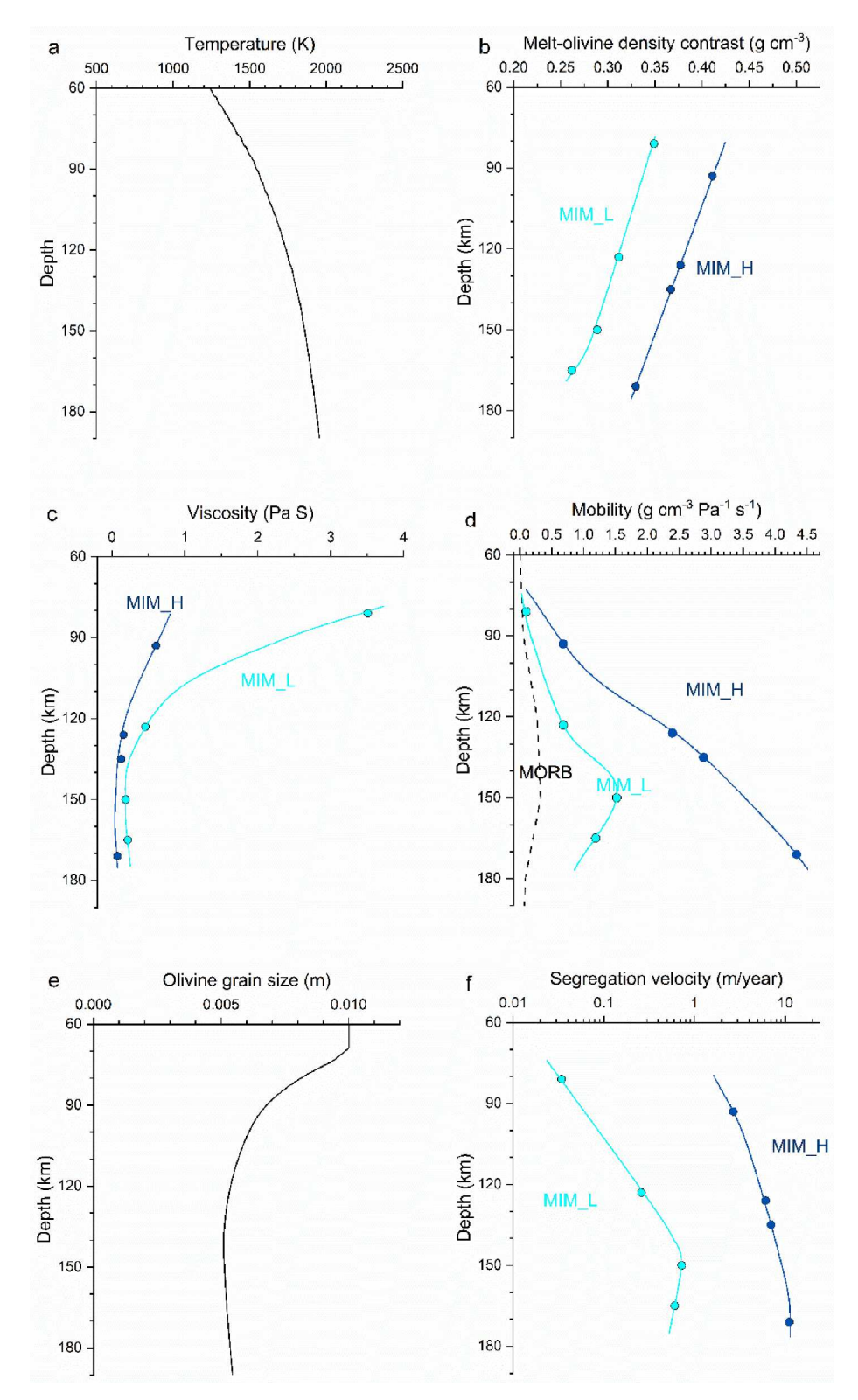


Fig. 4. (a) Geotherm beneath the mid-aged plate (70Ma, Sakamaki et al., 2013). (b) Melt and olivine density contrasts along the geotherm in Fig. 4a based on melt density model by (Ueki and Iwamori, 2016) and elasticity data of olivine by Zhang and Bass (2016). (c) Viscosity of the MIM\_L and MIM\_H along the geotherm in Fig. 4a. (d) Mobility of MIM\_L and MIM\_H along the geotherm in Fig. 4a, mobility of MORB melt is also shown for comparison (Sakamaki et al., 2013). (e) Grain size of olivine in the oceanic asthenosphere beneath plates with 10 cm/yr moving speed (Ramirez et al., 2023). (f) Segregation rate of MIM\_L and MIM\_H along the geotherm in Fig. 4a in a mantle with the grain size distribution shown in Fig. 4e, assuming a melt fraction of 0.1 vol%.

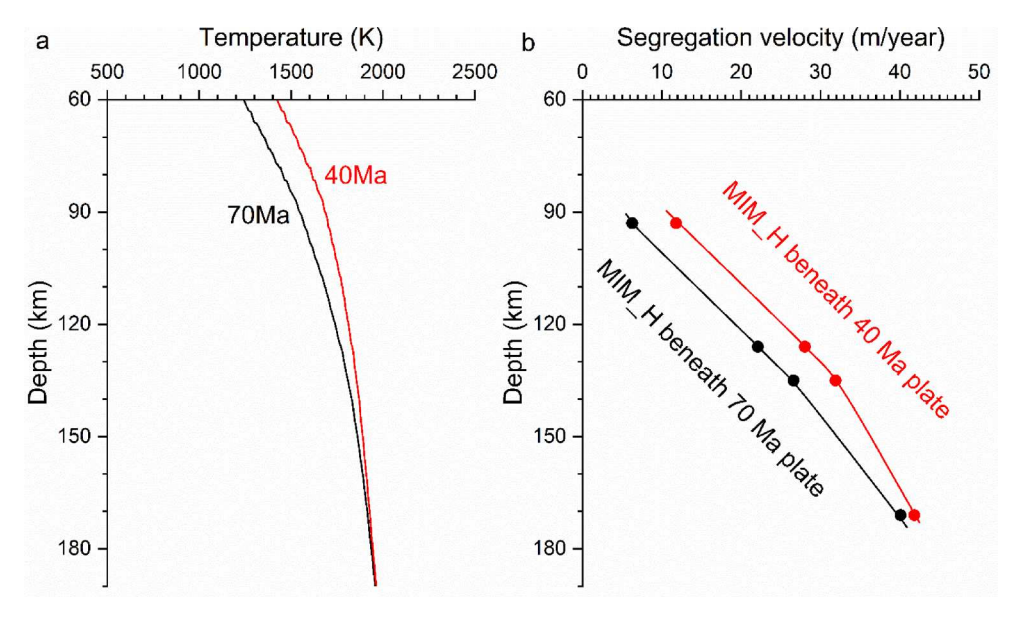


Fig. 5. a) Geotherms beneath a 40 Ma old oceanic plate and 70 Ma old oceanic plate (Sakamaki et al., 2013). b) Melt segregation velocity of mantle incipient melt with 4 wt% water along 2 different geotherms assuming 0.1 vol% melt fraction.

minimum at  $\sim$ 150 km (Fig. 4c). For a typical oceanic asthenosphere with 50–200 ppm water, the mantle incipient melt is estimated to contain 0.5–3.8 wt.% water when melt fraction is close to 0, and contain 0.4–3.2 wt.% water when melt fraction reaches 0.1 vol.% (Tenner et al., 2009). Given the availability of viscosity data for MIM\_L and MIM\_H up to  $\sim$ 6 GPa, we calculated mobility and segregation velocity of 0.1 vol% mantle incipient melts with 1.8 wt.% water and 4.0 wt.% water (Fig. 4).

Melt mobility is defined as the ratio of the melt-rock density contrast to the melt viscosity (Connolly et al., 2009). Lower melt viscosity and higher density contrast result in higher melt mobility. As shown in Fig. 4b, the density of the MIM\_L is approximately 0.3–0.4 g/cm³ less than the surrounding upper mantle rock. Due to its lower viscosity and lower density (high density contrast), the MIM\_L and MIM\_H are 2–5 times and 10 times more mobile than the MORB melt (Fig. 4d) in the asthenosphere, respectively.

Although the hydrous mantle incipient melts are highly mobile at

asthenosphere P-T conditions, their upward movement is also affected by melt connectivity which is governed by the dihedral angle between the melts and their surrounding minerals. Small dihedral angles contribute to the interconnectivity of melts. The dihedral angle observed for the mantle incipient melt and peridotite system at 3 GPa is reported to be around 30° (Gardés et al., 2020). This angle is significantly less than the critical dihedral angle of 60° required for complete interconnection of melts at all melt fractions (Sundberg et al., 2010; Waff and Bulau, 1979). Indeed, Gardés et al. (2020) observed that all mantle incipient melts were interconnected at an extremely low melt fraction of only  $\sim$ 0.1 vol.%. Additionally, the dihedral angle in the Mg<sub>2</sub>SiO<sub>4</sub>-H<sub>2</sub>O system was observed to drop with pressure, decreasing from 30° at 3 GPa to only 10° at 6 GPa along a 1473 K isotherm (Yoshino et al., 2007). Based on these previous studies, despite the low melt fraction in the asthenosphere being on the order of ~0.1 vol.% (Chantel et al., 2016; Debayle et al., 2020; Gardés et al., 2020; Katsura et al., 2017), mantle

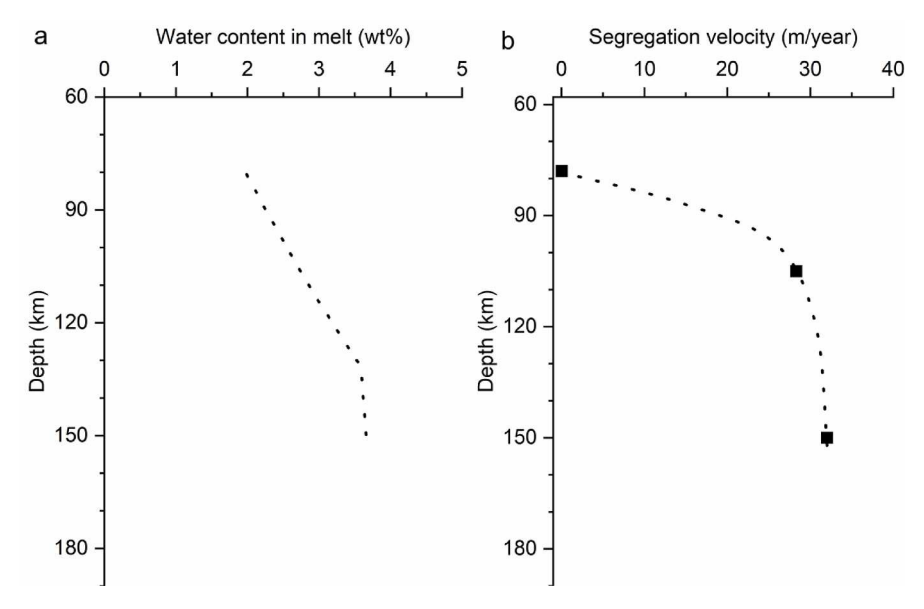


Fig. 6. a) Water content variation with depth based on mineral/melt hydrogen partitioning coefficient constrained by Tenner et al. (2009) assuming water content of 200 ppm in the ambient bulk silicate mantle. b) Melt segregation velocity of mantle incipient melt with depth-dependent water content shown in Fig. 6a assuming a constant grain size in the mantle (10 mm), a melt fraction of 0.1 vol.% and a geotherm below a 70 Ma oceanic plate.

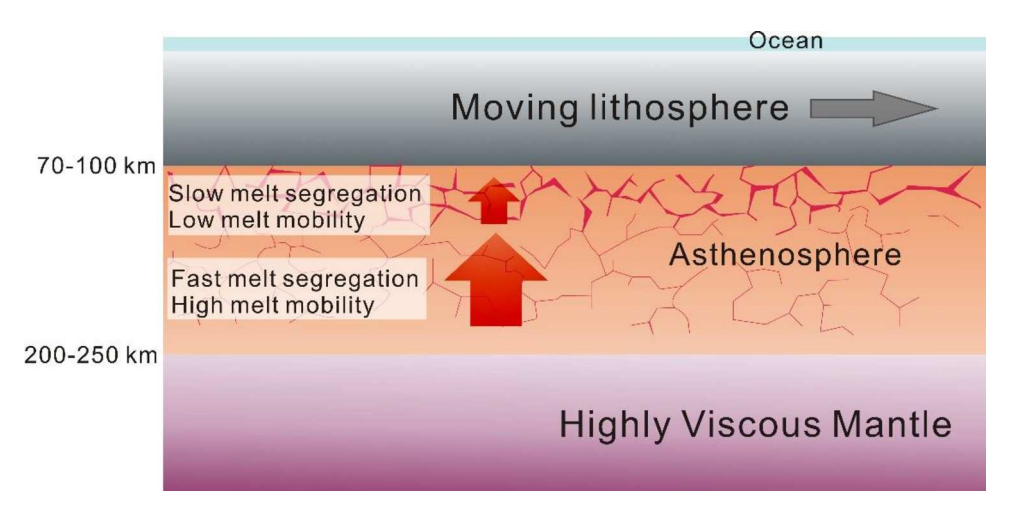


Fig. 7. Schematic figure showing the accumulation of mantle incipient melt at the top asthenosphere.

incipient melt is expected to be fully interconnected in the asthenosphere. We can further use Eq. (5) and (6) in the method section to calculate melt segregation velocity. As shown in Fig. 4f, the segregation velocity of mantle incipient melts MIM L increases with depth and peaks at 150 km, suggesting that hydrous mantle incipient melt with 1.8 wt.% water is expected to segregate easily from the asthenosphere at depths  $\geq$ 150 km. For both MIM\_L and MIM\_H, as melts ascend, the segregation velocity decreases quickly at depth shallower than 130-150 km, which results in melt accumulation near the top of the asthenosphere. Once the ascending hydrous mantle incipient melts cool down near the lithosphere-asthenosphere boundary, frozen melts can form and potentially can act as a low-permeability cap (Naif et al., 2013). For example, this cap is suggested to locate at 60 km, 70 km, 85 km, and 100 km depths under 30 Ma, 70 Ma, 100 Ma, and 150 Ma old plates, respectively (Katsura et al., 2017). Over the time, mantle incipient melts may accumulate from  $\sim$ 150 km depth to the shallower depth where they meet the permeability cap (Fig. 7). Our results are consistent with a recent global receiver-function study by Hua et al. (2023), which reported a lower base of the asthenospheric partial melting layer at approximately 150 km. As mantle incipient melts accumulate below the frozen cap, melt fraction is expected to reach the highest value, which is well explained by many local seismic studies suggesting strongest velocity reductions (up to -15 %) right below the lithosphere (Audhkhasi and Singh, 2022; Harmon et al., 2020; Mehouachi and Singh, 2018), As shown in Table 1. melt fractions at regions immediately adjacent to or at LAB are estimated to be 0.3-0.8 vol% globally, and up to 1.5 vol% in local areas. We further estimated the bulk mantle viscosity under the condition when small amount of mantle incipient melt presents (Fig. S3, Supplementary Text 2). The presence of 1 vol% melt would decrease mantle viscosity by ~30 %. Therefore, accumulation of partial melts at the LAB can help decouple the lithosphere from the asthenosphere, and promote plate movements on the Earth's surface (Ramirez et al., 2023).

We further calculated melt segregation velocity beneath oceanic plates with different ages. Beneath a hotter 40 Ma oceanic plate, melt is less viscous but with greater density contrast compared to the surrounding solid mantle. Melt is thus more mobile with a larger segregation velocity compared with those under a colder 70 Ma plate (Fig. 5), which is likely to result in more melt being transported to LAB. Thus, formation of a thicker LAB beneath younger plates is expected, agreeing well with what was observed by Mehouachi and Singh (2018).

Interestingly, the water partitioning coefficient between peridotite and melt is found to decrease from 0.01 at  $\sim$ 3 GPa to 0.005 at  $\sim$ 5 GPa, as pyroxenes become less abundant and less aluminous (Tenner et al., 2009). Assuming a constant bulk water content in the mantle, water content in the mantle incipient melt would decrease by half from  $\sim$ 150 km depth (5 GPa) to  $\sim$ 90 km depth (3 GPa). In a mantle with bulk water

content of 200 ppm, which is the upper bound of water content in the typical depleted oceanic asthenosphere (50–200 ppm), the mantle incipient melt contains 4 wt.% water at 5 GPa and 2 wt.% water at 3 GPa (Fig. 6a) (Tenner et al., 2009). As shown in Fig. 4, the mobility of the mantle incipient melt with  $\sim\!\!2$  wt.% water at 3 GPa is  $\sim\!\!20$  times less than the mobility of the melt with 4.0 wt.% water at 5 GPa. The segregation velocity of the mantle incipient melt with  $\sim\!\!2$  wt.% water at 3 GPa is also 1–2 orders of magnitude smaller than the melt with 4.0 wt.% water at 5 GPa (Fig. 6b). Therefore, the potentially less hydrous mantle incipient melt formed at shallower depths also contributes to reduced melt mobility and segregation velocity at the top of the asthenosphere.

In addition to water, the presence of high concentrations of CO $_2$  (up to 50 wt.%) has been suggested in the mantle incipient melt due to the highly incompatible nature of CO $_2$  at the asthenospheric P-T conditions (Dasgupta et al., 2013; Katsura et al., 2017). Future studies on hydrous carbonated melt will be beneficial for understanding the effect of CO $_2$  on melt transportation and migration in the asthenosphere. Compared to previous studies (e.g. Sakamaki et al. (2013), this study provides the first in-situ experimental constraint on the viscosity of hydrous basaltic melts at high P-T conditions, particularly with a chemical composition directly relevant to the melts potentially existing in the asthenosphere. The low viscosity and high mobility of hydrous mantle incipient melts are critical for future dynamic modeling of the long-term stability of such melts in the upper mantle.

#### 5. Conclusions

- 1) We present the first experimentally determined viscosity data for hydrous mantle incipient melts with 1.8–4.0 wt.% water content at 1.5–6.0 GPa along a 2100 K isotherm.
- 2) Viscosity of mantle incipient melts decreases with increasing water content. Additionally, viscosity of mantle incipient melts initially decreases with pressure and reaches a minimum at  $\sim$ 5 GPa.
- 3) Mantle incipient melts can easily migrate from the deeper asthenosphere toward the shallower part, but likely accumulate at the top of asthenosphere due to significant decrease in melt mobility and segregation velocity at shallower depths due to the decreased water content and pressure.

#### CRediT authorship contribution statement

**Wen-Yi Zhou:** Conceptualization, Writing – original draft, Visualization, Methodology, Investigation, Formal analysis, Data curation. **Ming Hao:** Writing – review & editing, Visualization, Formal analysis, Data curation. **Rostislav Hrubiak:** Writing – review & editing,

Resources, Methodology, Data curation. **Curtis Kenney-Benson:** Writing – review & editing, Resources, Data curation. **Jin S. Zhang:** Conceptualization, Resources, Funding acquisition, Formal analysis, Visualization, Writing – review & editing.

#### Declaration of competing interest

The authors declare that they have no known competing financial interests or personal relationships that could have appeared to influence the work reported in this paper.

#### Data availability

Data will be made available on request.

### Acknowledgement

This study was supported by NSF EAR1847707 (J.S.Z.) and the start up from Texas A&M University (J.S.Z.). The experiments were performed at HPCAT (Sector 16), Advanced Photon Source (APS), Argonne National Laboratory. HPCAT operations are supported by DOE-NNSA's Office of Experimental Sciences. We thank Man Xu for helpful discussions with experimental setup, and Andrew Mott for the assistance of EPMA experiments. The Advanced Photon Source is a U.S. Department of Energy (DOE) Office of Science User Facility operated for the DOE Office of Science by Argonne National Laboratory under Contract No. DE-AC02-06CH11357.

#### Supplementary materials

Supplementary material associated with this article can be found, in the online version, at doi:10.1016/j.epsl.2024.118833.

#### References

- Audhkhasi, P., Singh, S.C., 2022. Discovery of distinct lithosphere-asthenosphere boundary and the Gutenberg discontinuity in the Atlantic Ocean. Sci. Adv. 8 (24), eabn5404 v.
- Bonechi, B., Stagno, V., Kono, Y., Hrubiak, R., Ziberna, L., Andreozzi, G.B., Perinelli, C., Gaeta, M., 2022. Experimental measurements of the viscosity and melt structure of alkali basalts at high pressure and temperature. Sci. Rep. 12 (1), 2599 v.
- Chantel, J., Manthilake, G., Andrault, D., Novella, D., Yu, T., Wang, Y., 2016. Experimental evidence supports mantle partial melting in the asthenosphere. Sci. Adv. 2 (5), e1600246 v.
- Connolly, J.A., Schmidt, M.W., Solferino, G., Bagdassarov, N., 2009. Permeability of asthenospheric mantle and melt extraction rates at mid-ocean ridges. Nature 462 (7270), 209–212 v.
- Dasgupta, R., Mallik, A., Tsuno, K., Withers, A.C., Hirth, G., Hirschmann, M.M., 2013. Carbon-dioxide-rich silicate melt in the Earth's upper mantle. Nature 493 (7431), 211–215 v.
- Debayle, E., Bodin, T., Durand, S., Ricard, Y., 2020. Seismic evidence for partial melt below tectonic plates. Nature 586 (7830), 555–559 v.
- Drewitt, J.W., Walter, M.J., Brodholt, J.P., Muir, J.M., Lord, O.T., 2022. Hydrous silicate melts and the deep mantle H2O cycle. Earth Planet. Sci. Lett. 581, 117408 v.
- Freitas, D., Manthilake, G., Chantel, J., Bouhifd, M.A., Andrault, D., 2019. Simultaneous measurements of electrical conductivity and seismic wave velocity of partially molten geological materials: effect of evolving melt texture. Phys. Chem. Miner. 46, 535–551 v.
- Freitas, D., Manthilake, G., Schiavi, F., Chantel, J., Bolfan-Casanova, N., Bouhifd, M.A., Andrault, D., 2017. Experimental evidence supporting a global melt layer at the base of the Earth's upper mantle. Nat. Commun. 8 (1), 2186 v.
- Gardés, E., Laumonier, M., Massuyeau, M., Gaillard, F., 2020. Unravelling partial melt distribution in the oceanic low velocity zone. Earth Planet. Sci. Lett. 540, 116242 v.
- Harmon, N., Rychert, C.A., Kendall, J.M., Agius, M., Bogiatzis, P., Tharimena, S., 2020. Evolution of the oceanic lithosphere in the equatorial Atlantic from Rayleigh wave tomography, evidence for small-scale convection from the PI-LAB experiment. Geochem. Geophys. Geosyst. 21 (9), e2020GC009174 v.
- Hua, J., Fischer, K.M., Becker, T.W., Gazel, E., Hirth, G., 2023. Asthenospheric low-velocity zone consistent with globally prevalent partial melting. Nat. Geosci. 16 (2), 175–181 v.

- Katsura, T., Baba, K., Yoshino, T., Kogiso, T., 2017. Electrical conductivity of the oceanic asthenosphere and its interpretation based on laboratory measurements. Tectonophysics V 717, 162–181.
- Kawakatsu, H., Kumar, P., Takei, Y., Shinohara, M., Kanazawa, T., Araki, E., Suyehiro, K., 2009. Seismic evidence for sharp lithosphere-asthenosphere boundaries of oceanic plates. Science (1979) 324 (5926), 499–502 v.
- Kohn, S., 2000. The dissolution mechanisms of water in silicate melts; a synthesis of recent data. Mineral. Mag. 64 (3), 389-408 v.
- Kono, Y., Irifune, T., Higo, Y., Inoue, T., Barnhoorn, A., 2010. P V T relation of MgO derived by simultaneous elastic wave velocity and in situ X-ray measurements: a new pressure scale for the mantle transition region. Phys. Earth Planet. Interiors 183 (1-2), 196–211 v.
- Kono, Y., Park, C., Kenney-Benson, C., Shen, G., Wang, Y., 2014. Toward comprehensive studies of liquids at high pressures and high temperatures: combined structure, elastic wave velocity, and viscosity measurements in the Paris–Edinburgh cell. Phys. Earth Planet Interiors 228, 269–280 v.
- Li, X., Yuan, X., Kind, R., 2007. The lithosphere-asthenosphere boundary beneath the western United States. Geophys. J. Int. 170 (2), 700–710 v.
- Liebske, C., Schmickler, B., Terasaki, H., Poe, B.T., Suzuki, A., Funakoshi, K.-i., Ando, R., Rubie, D.C., 2005. Viscosity of peridotite liquid up to 13 GPA: implications for magma ocean viscosities. Earth Planet. Sci. Lett. 240 (3–4), 589–604 v.
- Mehouachi, F., Singh, S.C., 2018. Water-rich sublithospheric melt channel in the equatorial Atlantic Ocean. Nat. Geosci. 11 (1), 65–69 v.
- Mitchell, A.L., Gaetani, G.A., O'leary, J.A., Hauri, E.H., 2017. H 2 O solubility in basalt at upper mantle conditions. Contrib. Mineral. Petrol. 172, 1–16 v.
- Naif, S., Key, K., Constable, S., Evans, R., 2013. Melt-rich channel observed at the lithosphere-asthenosphere boundary. Nature 495 (7441), 356–359 v.
- Persikov, E.S., Bukhtiyarov, P.G., Sokol, A.G., 2018. Viscosity of haplokimberlitic and basaltic melts at high pressures: experimental and theoretical studies. Chem. Geol. 497, 54–63 v.
- Ramirez, F.D., Conrad, C.P., Selway, K., 2023. Grain size reduction by plug flow in the wet oceanic upper mantle explains the asthenosphere's low seismic Q zone. Earth Planet. Sci. Lett. 616, 118232 v.
- Romanowicz, B., 1995. A global tomographic model of shear attenuation in the upper mantle. J. Geophys. Res. Solid Earth 100 (B7), 12375–12394 v.
- Saal, A.E., Hauri, E.H., Langmuir, C.H., Perfit, M.R., 2002. Vapour undersaturation in primitive mid-ocean-ridge basalt and the volatile content of Earth's upper mantle. Nature 419 (6906), 451-455 v.
- Sakamaki, T., Suzuki, A., Ohtani, E., Terasaki, H., Urakawa, S., Katayama, Y., Funakoshi, K.-i., Wang, Y., Hernlund, J.W., Ballmer, M.D., 2013. Ponded melt at the boundary between the lithosphere and asthenosphere. Nat. Geosci. 6 (12), 1041–1044 v.
- Schmerr, N., 2012. The Gutenberg discontinuity: melt at the lithosphere-asthenosphere boundary. Science (1979) 335 (6075), 1480–1483 v.
- Shishkina, T.A., Botcharnikov, R.E., Holtz, F., Almeev, R.R., Jazwa, A.M., Jakubiak, A.A., 2014. Compositional and pressure effects on the solubility of H2O and CO2 in mafic melts. Chem. Geol. 388, 112–129 v.
- Sossi, P.A., Tollan, P.M., Badro, J., Bower, D.J., 2023. Solubility of water in peridotite liquids and the prevalence of steam atmospheres on rocky planets. Earth Planet. Sci. Lett. 601, 117894 v.
- Sundberg, M., Hirth, G., Kelemen, P., 2010. Trapped melt in the Josephine peridotite: implications for permeability and melt extraction in the upper mantle. J. Petrol. 51 (1–2), 185-200 v.
- Tenner, T.J., Hirschmann, M.M., Withers, A.C., Hervig, R.L., 2009. Hydrogen partitioning between nominally anhydrous upper mantle minerals and melt between 3 and 5 GPa and applications to hydrous peridotite partial melting. Chem. Geol. 262 (1–2), 42–56 v.
- Ueki, K., Iwamori, H., 2016. Density and seismic velocity of hydrous melts under crustal and upper mantle conditions. Geochem. Geophys. Geosyst. 17 (5), 1799–1814 v.
- Waff, H., Bulau, J.R., 1979. Equilibrium fluid distribution in an ultramafic partial melt under hydrostatic stress conditions. J. Geophys. Res. Solid Earth 84 (B11), 6109–6114 v.
- Wang, Y., Sakamaki, T., Skinner, L.B., Jing, Z., Yu, T., Kono, Y., Park, C., Shen, G., Rivers, M.L., Sutton, S.R., 2014. Atomistic insight into viscosity and density of silicate melts under pressure. Nat. Commun. 5 (1), 3241 v.
- Xu, M., Jing, Z., Van Orman, J.A., Yu, T., Wang, Y., 2020. Density of NaAlSi2O6 melt at high pressure and temperature measured by In-Situ X-ray microtomography. Minerals 10 (2), 161 v.
- Yasuda, A., Fujii, T., Kurita, K., 1994. Melting phase relations of an anhydrous mid-ocean ridge basalt from 3 to 20 GPa: implications for the behavior of subducted oceanic crust in the mantle. J. Geophys. Res. Solid Earth 99 (B5), 9401–9414 v.
- Yoshino, T., Nishihara, Y., Karato, S.-i., 2007. Complete wetting of olivine grain boundaries by a hydrous melt near the mantle transition zone. Earth Planet. Sci. Lett. 256 (3–4), 466–472 v.
- Zha, C.-S., Bassett, W.A., Shim, S.-H., 2004. Rhenium, an in situ pressure calibrant for internally heated diamond anvil cells. Rev. Sci. Instrum. 75 (7), 2409–2418 v.
- Zhang, J.S., Bass, J.D., 2016. Sound velocities of olivine at high pressures and temperatures and the composition of Earth's upper mantle. Geophys. Res. Lett. 43 (18), 9611–9618 v.